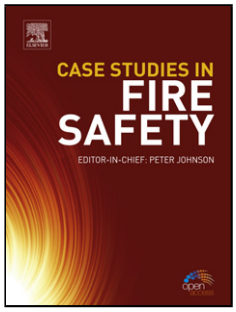

Title: Synergetic active corrosion protection of AA2024-T3 by 2D- anionic and 3D-cationic nanocontainers loaded with Ce and Mercaptobenzothiazole

Authors: M. Abdolah Zadeh, J. Tedim, M. Zhedlukevich, S. van der Zwaag, S.J. Garcia

PII: S0010-938X(17)30905-8
DOI: https://doi.org/10.1016/j.corsci.2018.02.018
Reference: CS 7375

To appear in:

Received date: 19-5-2017
Revised date: 13-1-2018
Accepted date: 13-2-2018

Please cite this article as: M.Abdolah Zadeh, J.Tedim, M.Zhedlukevich, S.van der Zwaag, S.J.Garcia, Synergetic active corrosion protection of AA2024-T3 by 2D- anionic and 3D-cationic nanocontainers loaded with Ce and Mercaptobenzothiazole, Corrosion Science https://doi.org/10.1016/j.corsci.2018.02.018

Synergetic active corrosion protection of AA2024-T3 by 2D-anionic and 3D-cationic nanocontainers loaded with Ce and Mercaptobenzothiazole

M. Abdolah Zadeh[a], J. Tedim [b], M. Zhedlukevich [b], S. van der Zwaag [a], S.J. Garcia [a,*]

[a] *Novel Aerospace Materials group, Faculty of Aerospace Engineering, Delft University of Technology, Kluyverweg 1, 2629 HS, Delft, The Netherlands*
[b]*CICECO - Aveiro Institute of Materials, Department of Materials and Ceramic Engineering, University of Aveiro, 3810-193 Aveiro, Portugal*

**Contact: e-mail: s.j.garciaespallargas@tudelft.nl*

Graphical abstract

<table>
<tr><td colspan="3">Epoxy–Amine coatings loaded with inhibiting nanoparticles on AA2024-T3 after 7 days immersion in NaCl</td></tr>
<tr><td> 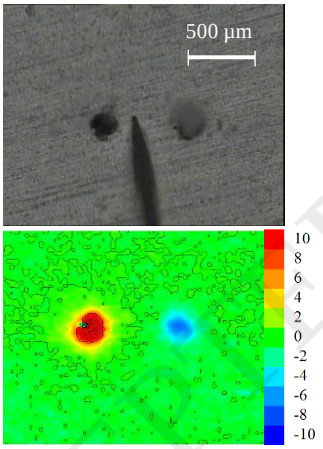
</td><td> 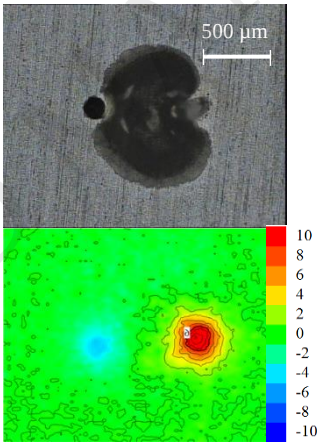
</td><td> 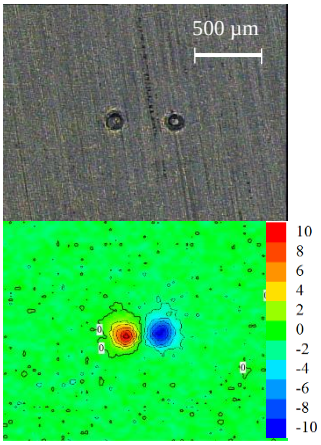
</td></tr>
<tr><td>Ce-Zeolite particles</td><td>MBT-LDH particles</td><td>Ce-Zeolite and MBT-LDH</td></tr>
</table>

Highlights

- LDH-MBT (2D) and NaY-Ce (3D) inhibitor-carrier particles were used.
- Inhibition synergy between a 2D and a 3D inhibitor-loaded carrier is demonstrated.
- Release kinetics from carriers are studied for a range of pH and NaCl concentrations.
- Inhibition in coatings depends on the ratio of 2D:3D particles used.
- For the studied system a 90:10 ratio (2D:3D) leads to the best inhibition efficiency.

ABSTRACT

In the current paper the corrosion inhibition synergy between Ce^{3+} loaded NaY-zeolite (NaY-Ce) and 2-Mercaptobenzothiazole (MBT) loaded Zn-Al layered double hydroxide (LDH-MBT) containers is presented. Solutions and water-borne epoxy coatings containing different ratios of the two loaded carriers were prepared and their protection of AA2024-T3 and damaged coatings characterized using global and local electrochemical techniques and other complementary tools. The coatings containing container-combinations showed exceptional corrosion protection over a broad range of NaY-Ce:LDH-MBT weight ratios, with 90:10 being the optimal. The current work landmarks the need for synergetic inhibiting studies devoted to carrier-inhibitor systems in coatings.

Selected keywords from Corrosion Science website

A. Organic coatings

A. Rare Earth elements

B. EIS

C. Interfaces

1. Introduction

Passive protective coatings are one of the most widespread approaches for corrosion protection of metallic substrates. Their protection mechanism is based on restricting the ingress of water and corrosive species to the metal-coating interface [1]. However, upon damage they fail to fulfil their protective function. In protective coatings, self-healing properties aiming at restoration of their corrosion protective function upon damage can be extrinsically introduced by incorporating corrosion inhibitors into the coating formulation [2-6]. For years, chromate compounds have been the most effective inhibitors for different metallic substrates. Yet, due to their toxicity and environmental regulations, their short and mid-term replacement by more benign inhibitors is necessary.

The quest for environmentally friendly alternatives to Cr(VI) compounds has revealed the beneficial aspects of rare earth metals (REM) such as cerium (Ce) in supressing corrosion of Al alloys [7, 8]. Nevertheless, so far no single-species replacement for chromates has been reported, from an equivalent performance perspective. The synergistic effects of inhibitor combinations can offer a promising route to outperform Cr(VI) species [9]. Rare earth organophosphates such as Ce dibutyl phosphate and Ce diphenyl phosphate with corrosion inhibition performances comparable to those of Cr(VI) compounds, are a new class of multifunctional corrosion inhibitors showing synergistic corrosion protection for AA2024-T3 [10-13]. Selective deposition of Ce on Cu-rich intermetallics and formation of an organic film by the organic part of the

inhibitor covering the entire surface is proposed as the most feasible mechanism for synergy of these compounds [13].

Despite the advances in the development of multifunctional inhibitors with synergistic properties, their direct implementation into coatings formulation may be associated with inevitable drawbacks such as chemical interactions between inhibitor and matrix followed by coating degradation and loss of inhibitor activity [14]. Entrapment of corrosion inhibitors in inert host structures, referred hereafter as micro- and nano-containers, not only can isolate active agents from coating components but can also control the release of the inhibitors. Zeolite and clay particles have lately attracted considerable interest as host structures for corrosion inhibitors due to their high loading capacity and ion-exchange capability [15, 16].

Zeolites are microporous aluminosilicate crystalline particles exhibiting a 3-dimensional (3D) framework which consists of sodalite cages connected through hexagonal prisms. Zeolites possess negative surface charge. This negative charge is compensated by cations loosely bonded to their framework [17, 18]. Cationic active species such as Ce^{3+} and La^{3+} ions can be entrapped within the structural cages of zeolite particles via cation exchange process [19-21]. The release process of the entrapped inhibitors in such containers is stimulated by corrosion activities involving pH changes and presence of cationic species (M^{n+} and H^{+}). Selective leaching of the inhibitive ions to the damage site can reinforce the protective oxide layer, guaranteeing the long-term protection for the metallic substrate. Combination of Ce^{3+} and La^{3+} loaded zeolites in the corrosion protective coatings has led to an improved active protection as a result of synergy between the two employed inhibitors [22]. Successive loading of two different inhibitors (Ce^{3+} and diethyldithiocarbamate (DEDTC)) in a single zeolite carrier has

also been reported with promising results based on a two steps/two triggers release concept [23]. The organic-inorganic hybrid coatings containing such carriers exhibited a noticeable improvement in active protection of AA2024 compared to the ones loaded with single inhibitor-loaded zeolites.

Layered double hydroxides (LDHs) are a class of anion-exchangeable clay particles consisting of stacks of positively charged 2-dimensional (2D) mixed-metal hydroxide layers. The positive charge of these frameworks is compensated by intercalation of anionic species between the hydroxide layers [24-26]. Inhibitor doped LDH particles can limit the release events to corrosion triggered phenomena such as pH changes or presence of anions released as a result of corrosion processes. Successful entrapment of anionic inhibitors in LDH has been reported in the literature [27-31]. Following the previous work with zeolites [23], both anionic and cationic inhibitors were recently loaded into single LDH showing slight improvements compared to LDHs loaded with either of inhibitors [32]. Although the synergistic effect of anionic inhibitors doped separately in LDH nano-containers has been addressed in a few publications [29], the potential synergy between the cationic inhibitor doped containers and the anionic inhibitors doped ones has not been reported yet.

In the present work, preparation and characterization of extrinsic healing corrosion protective coatings containing combination of cationic and anionic inhibitor doped containers is described. To this aim NaY zeolite and Zn-Al LDH were doped with Ce^{3+} and 2-Mercaptobenzothiazole as cationic and anionic inhibitors, respectively.Due to the different release mechanisms (pH range and anion/cation exchange) of the aforementioned inhibitors from their hosts (LDH or NaY-Zeolite) a synergetic effect can be expected. The morphology and composition of the micro-/ nano-containers were

studied using a combination of characterization techniques confirming successful loading of the employed inhibitors. Monitoring the inhibitor release profiles of the micro-/nano-containers as a function of NaCl concentration and solution pH provided valuable information on the possible synergistic corrosion protection mechanism. Furthermore, waterborne epoxy extrinsic healing coating containing individual inhibitor doped containers as well as their combination were prepared and evaluated using global and local electrochemical characterization techniques.

2. Experimental

2.1. Materials

Unclad AA2024-T3 was received from AkzoNobel and used as metallic substrate. A waterborne model epoxy-amine coating with fast drying at room temperature was kindly provided by Mankiewicz GmbH. Cerium(III) nitrate hexahydrate (99%, MW = 434.22 $g{\cdot}mol^{-1}$), 2-Mercaptobenzothiazole (97%, MW = 167.25 $g.mol^{-1}$) referred hereafter as MBT were purchased from Sigma-Aldrich and used without further purification as corrosion inhibitors. NaY zeolite (CBV 100, SiO_2/Al_2O_3 molar ratio: 5.1, Na_2O Weight %: 13.0) was purchased from Zeolyst International.

2.2. Nanoparticles synthesis and loading

NaY zeolite inhibitor loading

The single inhibitor doped Y zeolite was prepared via exchange of the available Na^+ cations in the Y zeolite cages with Ce^{3+}. The ion exchange process was carried out in a $Ce(NO_3)_3$ solution containing over 300% excess of Ce^{3+} cations with respect to cation exchange capacity (CEC) of NaY zeolite ensuring maximum exchange of Na cations with Ce^{3+} inhibitors [23]. The exchange process was conducted by addition of NaY

zeolite into a 0.3 M $Ce(NO_3)_3$ solution with volume/particle ratio of 20 $ml.g^{-1}$ at 60 ˚C. The Ce^{3+} doped NaY zeolites referred hereafter as NaY-Ce, were washed and filtered followed by drying at 60 °C for 24 h, yielding NaY zeolite with 12 ± 0.5 wt.% of Ce^{3+} cations.

Zn-Al LDH inhibitor loading

Inhibitor doped Zn-Al LHDs were prepared by co-precipitation followed by ion-exchange according to procedures described in literature [28]. In the first step, 0.5 M $Zn(NO_3)_2 \times 6H_2O$ and 0.25 M $Al(NO_3)_3 \times 9H_2O$ solution (V = 50 mL) was slowly added to 1.5 M $NaNO_3$ (V = 100 mL, pH 10) under vigorous stirring at room temperature, keeping the pH constant (pH 10 ± 0.5) by addition of 2 M NaOH solution. The resulting material was subjected to hydrothermal treatment (65 °C for 24 h) and consequently centrifuged and washed several times with boiled distilled water. A small fraction of LDHs was dried at 50 °C for characterization, while the remaining portion was used in the ion-exchange reaction [28, 29]. The nitrate-containing LDH precursor was dispersed in a solution of 0.1 M NaMBT (pH ≈ 10) under argon atmosphere, yielding LDH nano-containers with 30 ± 5 wt.% of MBT. The total amount of this solution (120 mL) was split into two portions of 60 mL to promote the exchange in two separate steps. Finally, the MBT-loaded LDHs were washed four times with boiled distilled water, frozen, and then dried by lyophilization at -78 °C [28, 29].

2.3 Pigment characterization

Morphology

Scanning electron microscopy (SEM): Particle morphology of the employed micro- and nano-containers were characterized using a high resolution JEOL SEM (JSM-

7500F) operating at 5 kV. Additionally, the composition of the inhibitor doped and un-doped containers were studied by energy-dispersive X-ray spectroscopy (EDS) using JSM-7500F operating at 15 kV.

Dynamic light scattering (DLS): The particle size distribution of the micro- and nano-containers and their zeta potentials were measured using a Malvern Zetasizer 4 instrument.

X-ray diffraction (XRD): The structure of the inhibitor doped and un-doped LDHs was studied by XRD. The measurements were performed using Philips X'Pert difractometer with Cu K_α radiation source.

Release kinetics

The release profiles of inorganic (Ce^{3+}) and organic (MBT) inhibitors from NaY and LDH containers were monitored by UV-Vis spectroscopy using a PerkinElmer Lambda 35 medium performance spectrophotometer in the spectral region of 220-400 nm. Unlike Ce^{3+}, the absorption spectra of MBT show two pH-sensitive peaks within the studied spectral range [33]. Therefore, MBT calibration curves were obtained at two different pH values; the natural pH of the solution and at pH = 10. The calibration was performed at the defined values using absorption peaks of λ = 318 nm and λ = 252 nm for MBT and Ce^{3+}, respectively [33, 34].

To study the release kinetics, the inhibitor doped containers were dispersed in an aqueous solution with volume/particle ratio of 400 ml g^{-1} under constant stirring. The effect of potential release triggering parameters were studied by systematic variation of NaCl concentration and pH values (NaCl concentrations = 0, 0.05 and 0.5 M, pH values

= 2, 4, 6.5 and 10). The suspensions were continuously stirred at 200 rpm. At definite time intervals, 2 ml samples were taken and filtered for analysis.

2.4. Coating preparation

Prior to coating application, AA2024-T3 panels of 3×4 cm^2 were ground mechanically using SiC paper (grade 1000) to remove the native oxide layer and further degreased with ethanol. The panels were then immersed in 2 M NaOH solution for 10 seconds and rinsed with double distilled water to increase the surface density of the hydroxyl groups (OH^-) on the AA2024-T3 substrates [35]. The cleaned and dried AA2024-T3 panels were then coated with the water-borne epoxy coatings.

The coating formulation consists of a waterborne epoxy emulsion and a solvent free amine hardener [36]. Prior to the addition of the hardener to the formulation, the resin was loaded with 10 wt% pigment (i.e. micro- and nano-containers) and mechanically stirred at 1000 rpm for 5 minutes to ensure full dispersion of the pigments in the resin. The hardener was then added to the mixture in a resin:hardener weight ratio of 0.7:1 and stirred manually. The resulting mixture was then cast on the cleaned AA2024-T3 panels using a bar coater with a nominal thickness of 50 µm. The coated samples were dried and cured at room temperature for 72 hour yielding coatings with an average dry thickness of 30 ± 5 µm (measured by Eddy current).

To evaluate the contribution of inhibitor doped micro- and nano-containers on the protective properties of the coatings, four types of formulations were prepared. The composition of the prepared coatings is summarized in table 1.

2.5. Coating characterization

Electrochemical procedures

Electrochemical impedance spectroscopy (EIS): The EIS measurements were carried out at room temperature in a three-electrode cell with a saturated calomel reference electrode (SCE), a Pt counter electrode and a selected coated specimen as working electrode in the horizontal position (exposed area of ca. 3.4 cm^2). A Faraday cage was employed to avoid the interference of external electromagnetic fields. A 0.05 M NaCl aqueous solution was used as testing electrolyte. The measurements were performed using a Gamry FAS2 Femtostat in the frequency range of 10^{-2}-10^5 Hz, with a 10 mV of sinusoidal perturbation, acquiring 7 data points per frequency decade. All the spectra were recorded at open circuit potential. The impedance plots were fitted using different equivalent circuits with the Echem Analyst™. To evaluate the corrosion inhibition at damaged sites by EIS, reproducible 3 mm long scratches with an average width of 30±5 μm were created using a CSM micro-scratch tester equipped with a sharp razor blade and an LED monitoring system to ensure the scratches reached the metallic surface.

In addition to the coating systems, bare AA2024-T3 panels were tested using EIS in a range of electrolytes containing $Ce(NO_3)_3$ and MBT in different molar ratios. The electrolytes were prepared using 0.05 M NaCl as background solution. The Ce:MBT molar ratio was systematically varied in the following manner: 99:1, 90:10, 75:25, 50:50 and 25:75.

Scanning vibrating electrode technique (SVET): The cathodic and anodic current densities were monitored using SVET over two circular artificial damages with an

average diameter of 150 ± 20 µm in the prepared coating systems. The measurements were performed using an Applicable Electronics Inc. equipment controlled with the ASET software from ScienceWares (USA) in a cell containing 5 ml of 0.05 M NaCl solution. The SVET maps were obtained by vibrating a microelectrode with a 20-30 µm spherical platinum black tip at amplitude of 20 µm, at an average distance of 100 µm above the sample surface. The scans consisted of 60 × 60 points over an exposed surface area of 4 × 4 mm^2.

3. Results & Discussion

3.1. Ce and MBT corrosion inhibitors compatibility

Ground and cleaned AA2024-T3 panels were tested using EIS in a range of 0.05 M NaCl solutions containing no inhibitor, 1 mM $Ce(NO_3)_3$, 1 mM MBT and 0.5 mM $Ce(NO_3)_3$+ 0.5 mM MBT. The EIS spectra of the AA2024-T3 panels after 1 h exposure to the test electrolytes and evolution of the R_{ct} (charge transfer resistance) are presented in Figure 1. As shown in Figure 1 a, the sample exposed to the inhibitor free electrolyte exhibited two time constants in the mid and low frequency ranges corresponding to the electrochemical processes occurring at the interface and mass transport controlled reactions, respectively [13]. However, addition of corrosion inhibitors to the test solution resulted in a significant increase in the |Z| values in both mid and low frequencies, with the occurrence of a single time constant possibly ascribed to the native oxide layer, confirming the effective corrosion inhibition provided by the employed inhibitors (Figure 1 a). The sample exposed to the combination of the two inhibitors exhibited the highest |Z| value at low frequencies suggesting improved corrosion protection due to the combination and potential synergy between Ce^{3+} and MBT.

To get an insight into the performance and possible inhibition mechanism of the combined inhibitors, the EIS spectra of the AA2024-T3 panels in different test electrolytes were monitored for 2 days. The EIS spectra were fitted using the protocol for most probable electrochemical circuit (MPEC) reported previously [12]. The evolution of the R_{ct} of the tested samples over 2 days of exposure are presented in Figure 1 b. The inhibitor free sample showed the lowest R_{ct} associated with the highest corrosion rate during the course of the measurement. Addition of Ce^{3+} led to a gradual and yet a significant increase in the R_{ct} of the AA2024-T3 panel. The progressive build-up in v in presence of Ce^{3+} can be explained by the protection mechanism of this REM inorganic inhibitor. The Ce^{3+} cation is believed to suppress corrosion of AA2024-T3 by gradual formation of an insoluble hydroxide or oxide layer on cathodic sites (e.g. S-phase intermetallics) of AA2024-T3 [7, 37, 38]. In contrast to Ce^{3+}, MBT provided a quick protection due to different inhibition mechanism i.e. adsorption on both aluminum oxide and aluminum surfaces especially on the copper rich domains [39, 40]. The combined inhibitor system yielded a fast and yet slightly higher protection than pure MBT and Ce^{3+}. The higher R_{ct} values might be attributed to the oxygen scavenging potential of the following reaction although more dedicated research is necessary to confirm this process:

$$2Ce^{4+} + 2HS - C_7H_3NS \xrightarrow{O_2} 2Ce^{3+} + SNH_3C_7 - S - S - C_7H_3NS \qquad \text{Eq. 1}$$

Corrosion of AA2024-T3 in chloride containing aerated solutions yields a range of pH values favored by different Ce species such as Ce^{3+} and Ce^{4+} [7]. Oxidation of free thiol groups by Ce^{4+} is a well-known reaction used for rapid and sensitive determination of

thiol in biological systems [41] yielding Ce^{3+} species. Consumption of oxygen in Eq. 1 alongside with the regeneration of Ce^{3+} cations can limit the cathodic reactions (OH^- evolution) and ultimately aluminum dissolution. Hence, Eq. 1 might offer an explanation for the improved performance of the combined inhibitor system compared to the pure inhibitors.

The tested samples were further studied using SEM/EDS to unravel their potential morphological and compositional differences. As Figures 2 a and b show a continuous cerium oxide layer covered the sample exposed to pure Ce^{3+} solution. The AA2024-T3 panel exposed to pure MBT solution showed several sulfur-rich strands on sample's surface (Figure 2 c and d). The sample exposed to the combined inhibitor system illustrated a combination of the two pure systems, i.e. a continuous cerium oxide layer with sulfur-rich strands on top. Yet, an additional feature was visible on this set of samples. Ceria particles were found in close vicinity of the sulfur-rich strands/rods (Figures 2 e and f).

3.2. Ce and MBT corrosion inhibitors ratio optimization in solution

The effect of inorganic (Ce^{3+}) and organic (MBT) inhibitors concentration on the active protection of the AA2024-T3 panels was investigated by systematic variation of Ce^{3+}:MBT molar ratio (99:1, 90:10, 75:25, 50:50, 25:75) in 0.05 M NaCl solution. The evolution of the R_{ct} of AA2024-T3 panels in solutions with different Ce^{3+}:MBT molar ratios is presented in Figure 3. As Figure 3 shows at the early stages of the measurement (i.e. 1 h), the samples exposed to 50:50 and 75:25 molar ratios of Ce^{3+}:MBT exhibited the highest R_{ct} values. The R_{ct} of all the other tested ratios were equivalent to that of pure MBT. Upon longer exposure, the Ce^{3+}:MBT molar ratio dependence of the R_{ct}

values diminished, so that after 1 day all the tested samples exhibited R_{ct} in the same range.

The results presented in Figure 3 show that despite the equivalent performance of the different Ce^{3+}:MBT molar ratios upon long exposure times (i.e. > 1 day), the fast and efficient active protection of AA2024-T3 can only be achieved within a narrow Ce^{3+}:MBT molar ratio range (50:50 and 75:25) with 50:50 being the optimum tested ratio.

3.3. Corrosion inhibition from loaded nanocarriers

The solution based EIS measurements showed that combining Ce^{3+} and MBT as inorganic and organic inhibitors not only does not deteriorate inhibition efficiency of the single inhibitors but also can lead to improved active protection of AA2024-T3 panels as a result of possible synergy between the two inhibitors. Therefore, a combination of Ce^{3+} and MBT can be incorporated into coating formulations to impart healing properties. Such coatings, referred hereafter as extrinsic healing corrosion protective coatings were prepared as described in the experimental section and tested using buld and local electrochemical procedures. To prevent coating instability and inhibitor deactivation [14] Ce^{3+} and MBT were entrapped in ion-exchange host structures (i.e. zeolite and LDH) prior to incorporation to the coating formulation.

NaY Zeolite

The morphology and composition of the undoped and Ce-doped NaY zeolites were studied using SEM/EDS (Figure 4). The SEM micrographs of NaY and NaY-Ce particles exhibited well-defined 3-dimensional (3D) crystals with an average diameter

of < 1µm. The EDS profile of NaY micro-containers (Figure 4 a) showed a distinct peak at 1.04 keV associated with the exchangeable Na cations in Y zeolite cages [42]. Substitution of Na with Ce cations in NaY-Ce led to compositional changes confirmed by a substantial decrease in the Na content (from 9.6 ± 0.2 wt.% to 3.1 ± 0.1 wt.%) and appearance of the characteristic peaks of Ce at 4.84, 5.27, 5.60 and 6 keV [42]. Presence of Na characteristic peak in NaY-Ce EDS spectrum indicates incomplete exchange process. The incomplete exchange of Na by Ce cations in NaY-Ce can be attributed to the size limitation of sodalite cages to fit in the hydrated Ce cations. The elemental analysis of NaY-Ce particles by EDS demonstrated successful loading of 12 ± 0.5 wt.% of Ce in Y zeolite. The obtained values are in agreement with ICP-OES analysis of remnant doping solutions yielding 11.2 ± 0.5 wt.% of Ce in NaY zeolites [42].

The effect of Ce doping on size distribution of NaY zeolite containers was further investigated by DLS (Figure 4 b). The size distribution of NaY zeolites is strongly affected by their zeta potential. High zeta potential values (either positive or negative) can stabilize particle dispersion by prevention of agglomerate formation as a result of electrostatic repulsion. NaY zeolite particles possess a negative surface charge due to isomorphous substitution of alumina by silica resulting in zeta potential values of -47.5 mV. Exchanging monovalent Na cations by trivalent Ce cations shifted the zeta potential of NaY-Ce particles towards more positive values (-37.9 mV). Yet, the obtained values were still negative enough to prevent agglomeration of NaY-Ce particles. The size distribution of NaY and NaY-Ce particles exhibited single peaks centred at 520 ± 50 and 560 ± 50 nm, which are in agreement with the size of particles observed by SEM.

LDH

LDH materials were characterized, before and after intercalation of corrosion inhibitor by XRD and the results are in agreement with previous works [32]. The replacement of NO_3^- by MBT in LDH nano-containers was confirmed by an increase in the gallery height from 0.42 nm to 1.72 nm [32].

morphology of the un-doped and MBT-doped Zn-Al LDHs was also evaluated using SEM. The SEM micrographs of the un-doped (Figure 5 a) and MBT-doped LDHs (Figure 5 b) showed that the prepared LDHs exhibited a 2-dimensional (2D) i.e. plate-like morphology which is retained upon anion-exchange, as reported in the literature [29]. The measured zeta potential for the LDH-MBT was +31.8 mV pointing to the low agglomeration potential of such particles in aqueous solutions.

3.4. Release of corrosion inhibitors from nanocarriers

The employed NaY and LDH nano-containers are cation- and anion-exchange compounds, respectively. Therefore, the doped inhibitors i.e. Ce^{3+} and MBT will only be released in presence of cationic and anionic species. Considering chloride concentration and pH changes as relevant corrosion triggering parameters, their effect on the release kinetics of the inhibitors from nano-containers was monitored by UV-Vis spectrophotometry. To this aim the relevant calibration curves were obtained using five standard solutions of known concentrations yielding molar absorptivity constants (ε) of 1.29, 0.047 and 0.054 $M^{-1}.cm^{-1}$ for Ce, MBT at neutral pH and MBT at pH = 10, respectively. The correlation coefficient of the calibration curves in all the cases was higher than 0.999. The obtained ε values were employed to calculate the released inhibitor concentration using Beer-Lambert's law [43].

$$A = \varepsilon l c \qquad \text{Eq. 2}$$

Where ε, l and c stand for molar absorptivity constant, pass length through the sample and inhibitor concentration, respectively.

The evolution of Ce^{3+} concentration in solutions with different NaCl concentrations (0, 0.05 and 0.5 M NaCl) and various pH values (2, 4, 6.5 and 10) is presented in Figure 6. The release profiles of Ce^{3+} from NaY-Ce micro-containers exhibited similar patterns, yet the amount of the leached inhibitor varied as a function of solution concentration and pH. As Figure 6 shows, in the early stages of the exposure the release process took place rapidly increasing the concentration of Ce^{3+} within 30 minutes in the solution. Upon reaching the chemical ion-exchange equilibrium [29], no significant changes in Ce^{3+} concentration were observed. While no release of Ce^{3+} to cation free DI water was detected, increasing the NaCl concentration from 0.05 M to 0.5 M boosted the release process (from 0.03 mM Ce in 0.05 M NaCl to 0.4 mM Ce in 0.5 M NaCl) confirming cation-exchange triggered release of the doped inhibitor from the micro-containers (Figure 6 a). The release profiles obtained at different pH values exhibited the same features i.e. fast release followed by stabilization of Ce^{3+} concentration upon longer exposure times. However, the extent of release was strongly influenced by solution pH (Figure 6 b). At pH = 10 no Ce^{3+} was detected in the solution during the test period. A gradual decrease in pH initiated the release process so that at pH 6.5 and 4, the Ce^{3+} plateau concentration was found to be 0.027 and 0.046 mM, respectively. A further decrease in pH down to a value of 2 intensified the release process yielding Ce^{3+} plateau concentration of 0.71 mM. The higher content of H^+ cations associated with lower pH values not only stabilizes Ce^{3+} species in the solution [44] but also provides the potential cations for cation-exchange process and release of the doped Ce^{3+} inhibitors.

In analogy to the Ce^{3+} release from NaY-Ce micro-containers, the content of the organic inhibitor (MBT) leached out of LDH nano-containers was strongly influenced by NaCl concentration and solution pH (Figure 7). An increase in the content of the anions present in the solution either in the form of chloride or hydroxide boosted MBT release from LDH nano-containers. A ten-fold increase in the chloride anions concentration shifted the MBT plateau concentration from 2.4 mM to 5 mM (Figure 7 a). Similarly, an increase in solution pH from 2 to 10 moved the plateau concentration from 0.96 mM to 3.6 mM (Figure 7 b). In all tested solutions, apart from the solution at pH = 10, the plateau concentration was achieved within a few minutes, indicative of quickly reaching chemical ion-exchange equilibrium. In the alkaline NaCl solution with pH = 10, the MBT concentration plateau was only achieved after 24 h (Figure 7 c). As Figures 6 and 7 shows the concentration of the released Ce^{3+} and MBT in a 0.05 M NaCl solution in their optimal release condition (pH values of 2 and 10 for Ce^{3+} and MBT, respectively) corresponds to 0.71 and 3.6 mM, respectively. These values are in-line with the lower loading extent of Ce^{3+} in NaY zeolite (12%) compared to that of MBT in LDH nano-containers (30%).

3.5. Active corrosion protection of AA2024-T3 by loaded coatings

To evaluate the performance of the combined Ce^{3+} and MBT doped containers a range of waterborne epoxy coatings containing 10 wt% NaY, 10 wt% NaY-Ce, 10 wt% LDH-MBT and 5 wt% NaY-Ce + 5 wt% LDH-MBT were prepared. The active protection offered by the doped inhibitors was evaluated by creation of two circular defects with an average diameter of 150 µm reaching the metallic substrate. The EIS spectra after one week of immersion is presented in Figure 8. From an initial observation it was possible to identify three well-defined time constants already after 1 hour exposure to

the electrolyte. At 7 days immersion the three inhibited coatings show higher impedance values than that of the reference system without inhibitor (NaY). Moreover, the coating loaded with the two-carrier system (NaY-Ce+LDH-MBT) shows one order of magnitude higher impedance than that of the two individual carrier systems, thereby highlighting the very significant increase in protection offered by the combination of the two carriers doped with different inhibitors.

To quantify the level of inhibition and corrosion protection offered by the inhibitor doped containers the EIS spectra of the tested coating systems were fitted using equivalent circuits presented in Figure 9 a. In the equivalent circuits depicted, R_{sol}, R_{coat}, R_{oxide} and R_{ct} correspond to solution, coating pore, oxide and charge transfer resistances, respectively. CPE_{coat}, CPE_{oxide} and CPE_{dl} represent coating, oxide and double layer constant phase elements, respectively. As Figure 9 shows, the coating resistance of the waterborne epoxy coatings exhibit an initial decrease followed by stabilization of R_{coat}. Therefore, the evolution of R_{oxide} provides a qualitative estimation of the inhibition efficiency of the employed inhibitor-loaded containers. Initially NaY-Ce shows the highest R_{oxide} values, yet after 2 immersion days R_{oxide} of this coating system droped significantly reaching the R_{oxide} values of the LDH-MBT system. The coating system containing combined inhibitor doped containers (NaY-Ce + LDH-MBT) showed a more stable R_{oxide} which was maintained for a longer period. At long immersion times (1 week exposure to the electrolyte) the NaY-Ce+LDH-MBT containing system showed the highest R_{oxide} values, hinting at synergy between the two inhibitors in the tested coating systems.

Additionally, the equivalent circuits provide information on the charge transfer resistance (R_{ct}) of the coating systems which can directly be correlated to the active protection provided by corrosion inhibitors using the following equation [45]:

$$\eta = \frac{CR_0 - CR_{inh}}{CR_0} \qquad \text{Eq. 3}$$

Where η, CR_0 and CR_{inh} represent inhibition efficiency and corrosion rate of the substrate in the defects of the coating with and without inhibitor respectively. It must be emphasised that the CR in this case is an approximation and includes the CR in the defect and in the micro-pores of the coating. The CR of the inhibitor-free and inhibitor containing coatings were calculated using the inverse of the charge transfer resistance (R_{ct}) of the corresponding coating systems. In the tested coatings the corrosion activity manifested by the third time constant in the EIS spectra was detected after few hours of immersion, hence the R_{ct} of them could be calculated using the EC presented in Figure 9. The R_{ct} of the coating systems after 1 and 7 days of exposure to the electrolyte, the fitting goodness (χ^2) and the calculated IEs are summarized in Table 2. The fitting goodness for all the coating systems was $\chi^2 < 1 \times 10^{-3}$.

To quantify any synergistic corrosion protection offered by combination of the inhibitor doped containers, the synergy parameter (S) was calculated using the following equation [45, 46]:

$$S = \frac{1 - \eta_{1+2}}{1 - \eta_{12}} \qquad \text{Eq. 4}$$

where η_{12} is the measured η for the coating loaded with two inhibitor doped containers and $\eta_{1+2}=(\eta_1+\eta_2) - (\eta_1 \times \eta_2)$. The values S > 1 indicate the synergistic behaviour of employed inhibitor combination.

As shown in Table 2, addition of the single inhibitor doped containers to the coating formulation led to a significant increase in the R_{ct} of the corresponding coating compared to the inhibitor free one, yielding η s of 0.95 and 0.49 for Ep-NaY-Ce and Ep-LDH-MBT, after 1 immersion day respectively. The coating containing the combined inhibitor doped containers exhibited an η of 0.79 which was slightly lower than that of Ep-NaY-Ce. However, over time the coating containing the combination of the inhibitor doped container outperformed the NaY-Ce containing one. The synergistic behaviour of the two inhibitor doped containers manifested by a S value of 2.14 was only observed after 1 week of exposure to the electrolyte.

In other words, upon long time exposure to the electrolyte (i.e. 1 week), Ep-LDH-MBT sample maintained its corrosion inhibition performance while the R_{ct} and therefore η of the Ep-NaY-Ce sample decreased dramatically; possibly due to depletion of accessible NaY-Ce containers from Ce^{3+} inhibitors. Yet, the coating containing the combined inhibitor doped containers exhibited the highest R_{ct} and η values, demonstrating the improvement in active protection of the substrate.

The observed synergy between the two inhibitor doped containers not only can be attributed to synergistic protection offered by the inorganic and organic inhibitors, but also can be ascribed to stimuli-triggered release of the inhibitors from the containers. The results presented in the release kinetics section revealed that while release of Ce^{3+} from NaY-Ce was boosted in acidic pHs, release of MBT from LDH-MBT was amplified at basic/alkaline pHs. Therefore by using the combination of the inhibitor

doped containers the release events can be expanded to a wide pH range (from very acidic to very basic) created by corrosion of AA2024-T3 in the chloride containing aerobic solutions. The released inhibitors can subsequently deactivate cathodic and anodic sites restricting Al dissolution.

To get a deeper insight into the synergism kinetics between the two inhibitor doped containers in the water based epoxy coatings, local electrochemical activities over the artificial defects of the coatings was monitored using SVET. The optical micrographs and SVET maps of the extrinsic healing corrosion protective epoxy coatings after 1 and 7 days of exposure to a 0.05 M NaCl solution are presented in Figure 10. It should be noted that the epoxy based coating without containers is not presented here due to its well-known total absence of active corrosion protection at damaged sites, not bringing additional insights to the data presented in Figure 10 and its interpretation. As Figure 10 shows, the coatings containing NaY-Ce (Figure 10 a) and LDH-MBT (Figure 10 b) exhibited corrosion activity manifested by anodic and cathodic current densities (red and blue regions, respectively) in the SVET maps and formation of corrosion products over the defects upon 1 day exposure to the electrolyte. The coating loaded with the combination of the inhibitor doped containers showed no electrochemical activity (Figure 10 e) after 1 day of exposure to the electrolyte, possibly due to suppression of corrosion activity by the combined inhibitors.

Prolonged exposure of the coating systems to the electrolyte resulted in severe corrosion of the substrates coated by both NaY-Ce and LDH-MBT loaded coatings. The fast evolution of the corrosion processes in these coating systems was demonstrated by well-defined anodic and cathodic regions as well as formation of blisters followed by coating delamination (Figures 10 b and d). Although, the coating containing the combined

inhibitor doped containers exhibited anodic and cathodic current density peaks after 7 days exposure to the electrolyte (Figure 10 f), the shiny surface of the defects suggested lower corrosion activity compared to the single inhibitor doped coatings. Moreover, it should be noted that the presence of corrosion products and delamination in the other two systems leads to an underestimation of the corrosion current densities at the bottom of the holes. Therefore, the values seen in figure 10b and 10d should be treated with care.

The differences in the extent of the active protection provided by loading the inhibitor doped containers in epoxy coatings was further investigated by performing line scans over the artificial defects using SVET. The ionic current density (i_{Ionic}) profiles of the tested coating systems are shown in Figure 11.

As Figure 11 a shows, at the early stages of the measurement (1 h immersion) no electrochemical activity was detected over the defects of the coating systems. Upon 1 day exposure the coating loaded with LDH-MBT (Figure 11 b) exhibited anodic (i_{anodic} = 12 µA.cm^2) and cathodic ($i_{cathodic}$ = -11.3 µA.cm^2) activities attributed respectively to dissolution of Al as a result of corrosion and reduction of oxygen on copper-rich regions. After 3 days, the corrosion processes were established in NaY-Ce loaded system (i_{anodic} = 17.35 µA.cm^2) and further evolved in LDH-MBT containing one (i_{anodic} = 28.5 µA.cm^2), yet the defects in the coating containing the combined inhibitor doped containers remained passive. Although corrosion of the defects in the later coating system started after 7 days of exposure to the electrolyte, both anodic and cathodic current densities were much lower than those of NaY-Ce loaded coating. Formation of a blister due to reduction of oxygen in the cathodic defect of LDH-MBT loaded coating interrupted the line scan at the same height (100 µm above the sample surface) as the

rest of the coatings. The results presented in Figures 10 and 11 revealed the improved performance of the combined inhibitor doped containers in supressing corrosion of coated AA2024-T3 panels at the defect site, further confirming the synergy between the employed inhibitors.

Optimization of NaY-Ce to LDH-MBT ratio

To find the optimum ratio of the inhibitor doped containers, a range of waterborne epoxy coatings containing different weight ratios of NaY-Ce:LDH-MBT (90:10, 75:25, 50:50 and 25:75) were prepared and tested using EIS. The active protection of the AA2024-T3 panels by the coating systems was evaluated by creating an artificial damage in the form of a 3 mm long and 30 µm wide scratch in the coatings prior to exposure to the electrolyte and fitting the EIS data by a three-time constant equivalent circuit. The EIS spectra and the evolution of oxide (R_{oxide}) and charge transfer ($R_{ct.}$) resistances of the tested coating systems are presented in Figure 12. As Figure 12 shows, the coating containing NaY-Ce + LDH-MBT with weight ratio of 25:75 exhibited the lowest Bode modulus (|Z|) in the tested frequency range over the course of the measurement (Figures 12 a and b). The rest of the coating systems showed comparable high frequency total impedances, indicating similar coating responses and slightly different low frequency |Z| to the one containing NaY-Ce + LDH-MBT in the weight ratio 90:10.

The R_{oxide} (Figure 12 c) of the coating systems showed a gradual increase over time due to release of the doped inhibitors, reinforcing of the protective oxide layer. The increased resistance of the oxide layer can lower the corrosion rate of epoxy coated AA2024-T3 panels. The reduced corrosion rate of the tested systems was reflected by the gradual increase in their $R_{ct.}$ (Figure 12 d). Among the tested coating systems the

ones containing NaY-Ce + LDH-MBT with weight ratio of 25:75 and 90:10 exhibited the lowest and highest R_{oxide} and $R_{ct.}$, respectively. This observation might be attributed to the fine balance between two competing phenomena i.e. release of the MBT from LDH-MBT and formation of the protective cerium hydroxide/oxide layer on the cathodic sites of AA2024-T3 activated by hydroxide groups.

Additionally, based on the results presented in release kinetics section, the maximum content of inhibitor leached out of the NaY-Ce and LDH-MBT containers corresponds to 0.65 ± 0.5 mM Ce^{3+} and 5.5 ± 0.5 mM MBT, respectively. Therefore, the released inhibitor molar ratio in the coating containing NaY-Ce + LDH-MBT in weight ratio of 90:10 might correspond to 1:1 Ce^{3+}:MBT molar ratio. The aforementioned molar ratio of the two inhibitors exhibited the highest R_{ct} in the solution-based tests even at the early stages of the measurement (Figure 3). Hence the highest R_{Oxide} and R_{ct} of the coating system containing 90:10 weight ratio of NaY-Ce + LDH-MBT is in agreement with the solution based tests.

5. Conclusions

In this study, the preparation and characterization of the inhibitor loaded NaY zeolite and LDH containers are described. Ce^{3+} and MBT were successfully loaded in NaY zeolite and LDH containers, yielding NaY-Ce and LDH-MBT with Ce^{3+} and MBT weight percentages of 12% and 30%, respectively. The inhibitor doped containers exhibited stimuli-triggered release phenomena. An increase in the concentration of the ions (Na^+ and Cl^-) in the test solution promoted the release of the inhibitors via ion-exchange process. The release of Ce^{3+} and MBT from NaY-Ce and LDH-MBT were boosted at low and high pH values, respectively. The combination of the two employed

inhibitors presented a constructive effect in the active protection of AA2024-T3 panels with 1:1 being the optimum Ce^{3+}:MBT molar ratio. Incorporation of the single inhibitor doped containers waterborne epoxy coating provided active protection for the coated AA2024-T3 substrates. Yet, the combination of the inhibitor doped containers in the aforementioned coatings led to an improvement in the active protection of the substrate, confirming the synergy between the two inhibitor doped containers. The active protection offered by the combination of the two inhibitor doped containers was affected by the weight ratio of the NaY-Ce to LDH-MBT in the coatings with 90:10 being the best ratio of the explored combinations. The current work landmarked the need for synergetic inhibiting studies devoted to carrier-inhibitor combinations focusing on the optimization of this concept but also addressing other relevant coating properties such as adhesion and mechanical performance.

Acknowledgments

MA, SvZ and SJG would like to acknowledge the Dutch National IOP program on self-healing materials for grant IOP-SHM-1028. JT and MZ would like to acknowledge the IF/00347/2013 grant from FCT. Additionally the authors would like to thank A. Bastos for his help and input during the SVET measurements.

References

[1] G.W. Walter, A critical review of the protection of metals by paints, Corrosion Science, 26 (1986) 27-38.
[2] R.T.M. van Benthem, W. Ming, G. de With, Self Healing Polymer Coatings, in: S. van der Zwaag (Ed.) Self Healing Materials, Springer Netherlands2007, pp. 139-159.
[3] A.E. Hughes, I.S. Cole, T.H. Muster, R.J. Varley, Designing green, self-healing coatings for metal protection, NPG Asia Mater, 2 (2010) 143-151.
[4] S.J. García, H.R. Fischer, S. van der Zwaag, A critical appraisal of the potential of self healing polymeric coatings, Progress in Organic Coatings, 72 (2011) 211-221.
[5] D.G. Shchukin, D. Borisova, H. Möhwald, Self-Healing Coatings, Self-Healing Polymers, Wiley-VCH Verlag GmbH & Co. KGaA2013, pp. 381-399.
[6] D.G. Shchukin, M. Zheludkevich, K. Yasakau, S. Lamaka, M.G.S. Ferreira, H. Möhwald, Layer-by-Layer Assembled Nanocontainers for Self-Healing Corrosion Protection, Advanced Materials, 18 (2006) 1672-1678.
[7] K.A. Yasakau, M.L. Zheludkevich, S.V. Lamaka, M.G. Ferreira, Mechanism of corrosion inhibition of AA2024 by rare-earth compounds, The Journal of Physical Chemistry B, 110 (2006) 5515-5528.
[8] S.J. García, J.M.C. Mol, T.H. Muster, A.E. Hughes, T.M.J. Mardel, H.T.T. Markely, J.H.W. de Wit, Advances in the selection and use of rare-earth based inhibitors for selfhealing organic coatings, Self-Healing Properties of New Surface Treatments, European Federation of Corrosion Series, Maney Publishing, UK, 2011, pp. 148–183.
[9] D. Snihirova, S.V. Lamaka, P. Taheri, J.M.C. Mol, M.F. Montemor, Comparison of the synergistic effects of inhibitor mixtures tailored for enhanced corrosion protection of bare and coated AA2024-T3, Surface and Coatings Technology, 303 (2016) 342-351.
[10] N. Birbilis, R. Buchheit, D. Ho, M. Forsyth, Inhibition of AA2024-T3 on a phase-by-phase basis using an environmentally benign inhibitor, cerium dibutyl phosphate, Electrochemical and solid-state letters, 8 (2005) C180-C183.
[11] T.A. Markley, M. Forsyth, A.E. Hughes, Corrosion protection of AA2024-T3 using rare earth diphenyl phosphates, Electrochimica acta, 52 (2007) 4024-4031.
[12] M. Forsyth, M. Seter, B. Hinton, G. Deacon, P. Junk, New'green'corrosion inhibitors based on rare earth compounds, Australian Journal of Chemistry, 64 (2011) 812-819.
[13] S. Garcia, T. Markley, J. Mol, A. Hughes, Unravelling the corrosion inhibition mechanisms of bi-functional inhibitors by EIS and SEM–EDS, Corrosion Science, 69 (2013) 346-358.
[14] M. Zheludkevich, Self-Healing Anticorrosion Coatings, Self-Healing Materials, Wiley-VCH Verlag GmbH & Co. KGaA2009, pp. 101-139.
[15] M. Abdolah Zadeh, S. Van Der Zwaag, S. Garcia, Routes to extrinsic and intrinsic self-healing corrosion protective sol-gel coatings: a review, Self-Healing Materials, 1 (2013) 1-18.
[16] M. Abdolah Zadeh, S. van der Zwaag, S.J. Garcia, Self-healing corrosion protective sol-gel coatings based on extrinsic and intrinsic healing approaches, Advances in Polymer Science, 273 (2016) 185–218.
[17] Zeolite Molecular Sieves: Structure, Chemistry, and Use D. W. Breck (Union Carbide Corporation, Tarrytown, New York) John Wiley and Sons, New York, London, Sydney, and Toronto. 1974. 771 pp.

[18] R. Xu, W. Pang, J. Yu, Q. Huo, J. Chen, Structural Chemistry of Microporous Materials, Chemistry of Zeolites and Related Porous Materials, John Wiley & Sons, Ltd. 2010, pp. 19-116.
[19] C. Motte, M. Poelman, A. Roobroeck, M. Fedel, F. Deflorian, M.G. Olivier, Improvement of corrosion protection offered to galvanized steel by incorporation of lanthanide modified nanoclays in silane layer, Progress in Organic Coatings, 74 (2012) 326-333.
[20] S.A.S. Dias, A. Marques, S.V. Lamaka, A. Simões, T.C. Diamantino, M.G.S. Ferreira, The role of Ce(III)-enriched zeolites on the corrosion protection of AA2024-T3, Electrochimica Acta, 112 (2013) 549-556.
[21] S.A.S. Dias, S.V. Lamaka, C.A. Nogueira, T.C. Diamantino, M.G.S. Ferreira, Sol–gel coatings modified with zeolite fillers for active corrosion protection of AA2024 Corrosion Science, (2012) 153-162.
[22] S.A.S. Diasa, S.V. Lamakab, T.C. Diamantino, M.G.S. Ferreira, Synergistic Protection against Corrosion of AA2024-T3 by Sol-Gel Coating Modified with La and Mo-Enriched Zeolites, J. Electrochem. Soc. , 161 (2014) C215-C222.
[23] E.L. Ferrer, A.P. Rollon, H.D. Mendoza, U. Lafont, S.J. Garcia, Double-doped zeolites for corrosion protection of aluminium alloys, Microporous and Mesoporous Materials, 188 (2014) 8-15.
[24] R.G. Buchheit, H. Guan, S. Mahajanam, F. Wong, Active corrosion protection and corrosion sensing in chromate-free organic coatings, Progress in Organic Coatings, 47 (2003) 174-182.
[25] H. McMurray, G. Williams, Inhibition of filiform corrosion on organic-coated aluminum alloy by hydrotalcite-like anion-exchange pigments, Corrosion, 60 (2004) 219-228.
[26] G. Williams, H.N. McMurray, Inhibition of filiform corrosion on polymer coated AA2024-T3 by hydrotalcite-like pigments incorporating organic anions, Electrochemical and solid-state letters, 7 (2004) B13-B15.
[27] M. Kendig, M. Hon, A hydrotalcite-like pigment containing an organic anion corrosion inhibitor, Electrochemical and solid-state letters, 8 (2005) B10-B11.
[28] S. Poznyak, J. Tedim, L. Rodrigues, A. Salak, M. Zheludkevich, L. Dick, M. Ferreira, Novel inorganic host layered double hydroxides intercalated with guest organic inhibitors for anticorrosion applications, ACS applied materials & interfaces, 1 (2009) 2353-2362.
[29] J. Tedim, S. Poznyak, A. Kuznetsova, D. Raps, T. Hack, M. Zheludkevich, M. Ferreira, Enhancement of active corrosion protection via combination of inhibitor-loaded nanocontainers, ACS applied materials & interfaces, 2 (2010) 1528-1535.
[30] T. Stimpfling, P. Vialat, H. Hintze-Bruening, P. Keil, V. Shkirskiy, P. Volovitch, K. Ogle, F. Leroux, Amino Acid Interleaved Layered Double Hydroxides as Promising Hybrid Materials for AA2024 Corrosion Inhibition, European Journal of Inorganic Chemistry, 2016 (2016) 2006-2016.
[31] M.F. Montemor, D.V. Snihirova, M.G. Taryba, S.V. Lamaka, I.A. Kartsonakis, A.C. Balaskas, G.C. Kordas, J. Tedim, A. Kuznetsova, M.L. Zheludkevich, M.G.S. Ferreira, Evaluation of self-healing ability in protective coatings modified with combinations of layered double hydroxides and cerium molibdate nanocontainers filled with corrosion inhibitors, Electrochimica Acta, 60 (2012) 31-40.
[32] J. Carneiro, A.F. Caetano, A. Kuznetsova, F. Maia, A.N. Salak, J. Tedim, N. Scharnagl, M.L. Zheludkevich, M.G.S. Ferreira, Polyelectrolyte-modified layered

double hydroxide nanocontainers as vehicles for combined inhibitors, RSC Advances, 5 (2015) 39916-39929.
[33] F. Li, X. Li, K. Ng, Photocatalytic degradation of an odorous pollutant: 2-mercaptobenzothiazole in aqueous suspension using Nd3+-TiO2 catalysts, Industrial & engineering chemistry research, 45 (2006) 1-7.
[34] P. Ruoff, A. Bjørnstad, M. Jakobsen, The complete UV–visible photoluminescence spectrum of aqueous Ce (III), Chemical physics letters, 291 (1998) 249-251.
[35] Ö. Özkanat, Molecular interfaces of coated aluminium, PhD thesis TUDelft, 2013.
[36] F. Maia, J. Tedim, A.D. Lisenkov, A.N. Salak, M.L. Zheludkevich, M.G.S. Ferreira, Silica nanocontainers for active corrosion protection, Nanoscale, 4 (2012) 1287-1298.
[37] A. Aldykiewicz, A. Davenport, H. Isaacs, Studies of the Formation of Cerium-Rich Protective Films Using X-Ray Absorption Near-Edge Spectroscopy and Rotating Disk Electrode Methods, Journal of the Electrochemical Society, 143 (1996) 147-154.
[38] V. Palanivel, Y. Huang, W.J. van Ooij, Effects of addition of corrosion inhibitors to silane films on the performance of AA2024-T3 in a 0.5 M NaCl solution, Progress in Organic Coatings, 53 (2005) 153-168.
[39] M. Ohsawa, W. Suëtaka, Spectro-electrochemical studies of the corrosion inhibition of copper by mercaptobenzothiazole, Corrosion Science, 19 (1979) 709-722.
[40] A.N. Khramov, N.N. Voevodin, V.N. Balbyshev, R.A. Mantz, Sol–gel-derived corrosion-protective coatings with controllable release of incorporated organic corrosion inhibitors, Thin Solid Films, 483 (2005) 191-196.
[41] G.-C. Han, Y. Peng, Y.-Q. Hao, Y.-N. Liu, F. Zhou, Spectrofluorimetric determination of total free thiols based on formation of complexes of Ce (III) with disulfide bonds, Analytica chimica acta, 659 (2010) 238-242.
[42] E.L. Ferrer, A.P. Rollon, H.D. Mendoza, U. Lafont, S.J. Garcia, Double-doped zeolites for corrosion protection of aluminium alloys, Microporous and Mesoporous Materials, 188 (2014) 8-15.
[43] K. Fuwa, B. Valle, The Physical Basis of Analytical Atomic Absorption Spectrometry. The Pertinence of the Beer-Lambert Law, Analytical Chemistry, 35 (1963) 942-946.
[44] S.A. Hayes, P. Yu, T.J. O'Keefe, M.J. O'Keefe, J.O. Stoffer, The Phase Stability of Cerium Species in Aqueous Systems I. E-pH Diagram for the Ce HClO 4 H 2 O System, Journal of the Electrochemical Society, 149 (2002) C623-C630.
[45] S. Kallip, A.C. Bastos, K.A. Yasakau, M.L. Zheludkevich, M.G. Ferreira, Synergistic corrosion inhibition on galvanically coupled metallic materials, Electrochemistry Communications, 20 (2012) 101-104.
[46] K. Aramaki, Effects of organic inhibitors on corrosion of zinc in an aerated 0.5 M NaCl solution, Corrosion science, 43 (2001) 1985-2000.

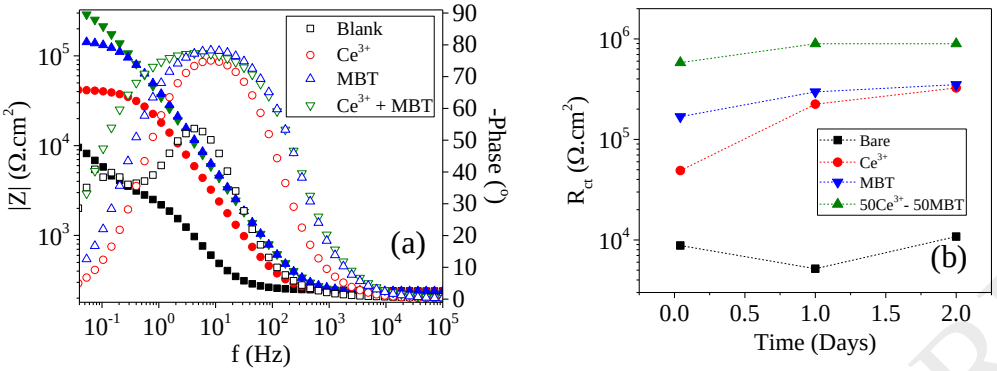

Figure 1. The EIS spectra after 60 minutes immersion (a) and evolution of the R_{ct} for AA2024-T3 panels exposed to inhibitor free (■), 1 mM Ce^{3+} (●), 1 mM MBT (▼) and 0.5 mM Ce^{3+} + 0.5 mM MBT (▲) containing 0.05 M NaCl (b).

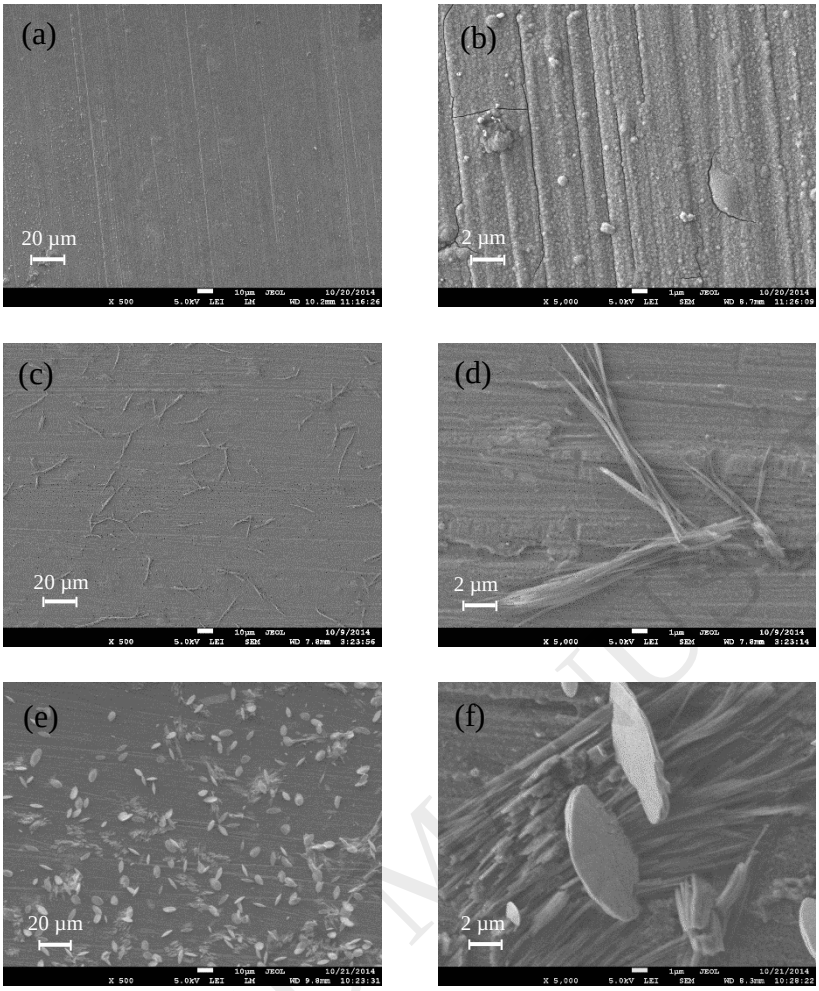

Figure 2. SEM micrographs of AA2024-T3 exposed for 14 days to 1 mM $Ce(NO_3)_3$at 500x (a) and 5000x (b), to 1 mM MBT at 500x (c) and 5000x (d) and to 0.5 mM $Ce(NO_3)_3$+ 0.5 mM MBT at 500x (e) and 5000x (f).

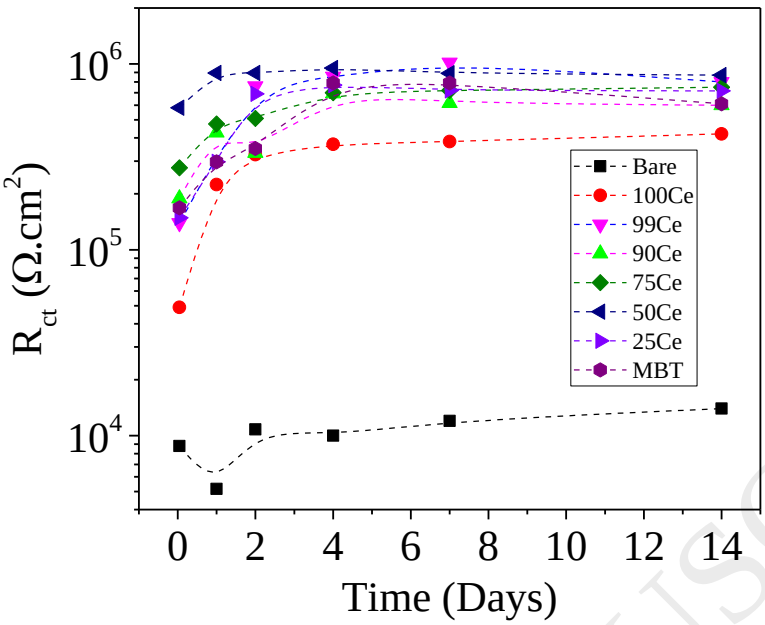

Figure 3. Evolution of the R_{ct} of AA2024-T3 panels in 0.05 M NaCl solution containing different Ce^{3+}:MBT molar ratios.

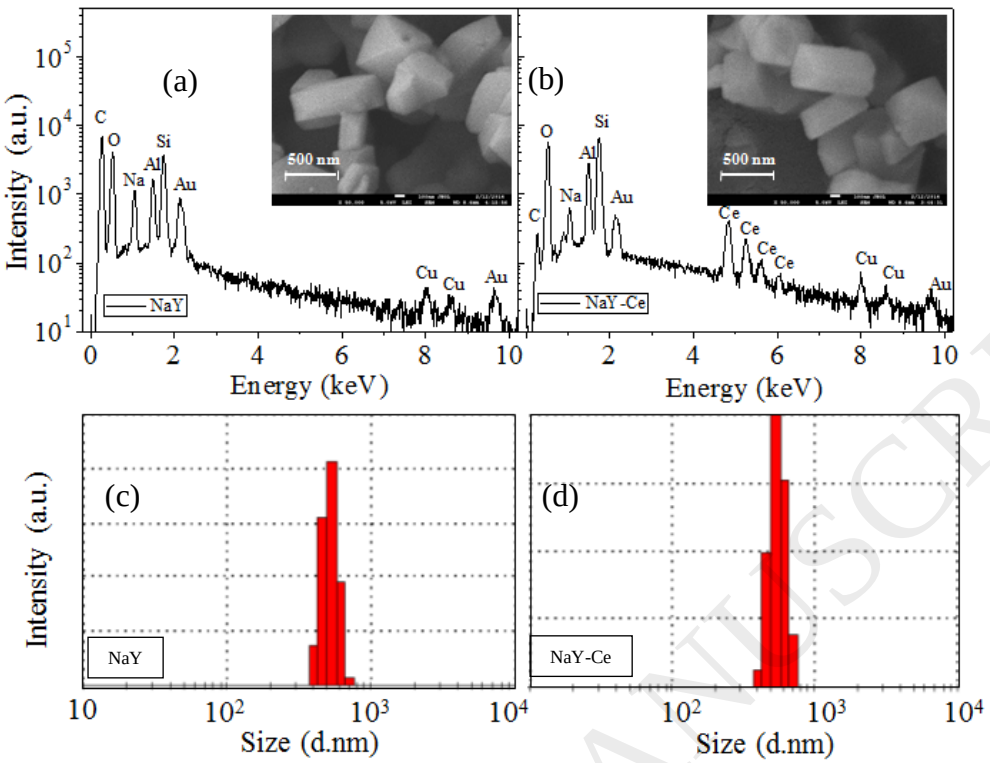

Figure 4. EDS spectra and SEM micrographs (picture inset) of NaY (a) and NaY-Ce and size distribution of NaY (c) and NaY-Ce particles (d).

(a) (b)

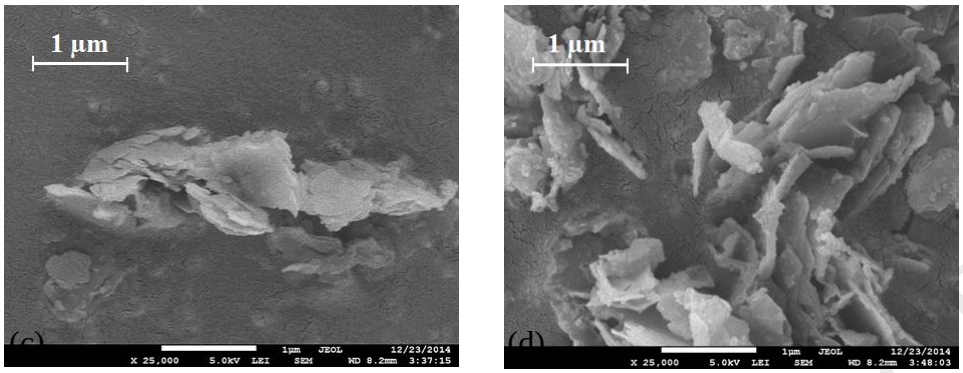

Figure 5. SEM micrographs of un-doped (a) and MBT-doped (b) Zn-Al LDHs at 25000x.

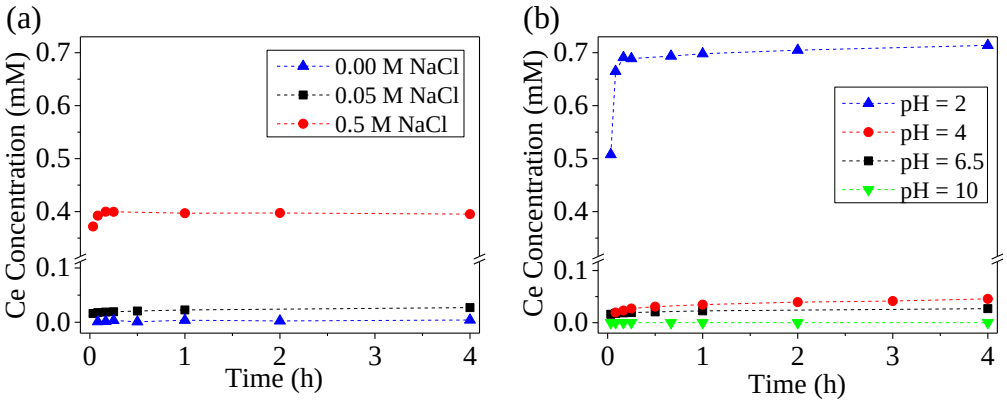

Figure 6. Ce^{3+} release profiles at neutral pH in different NaCl concentrations (a) and in 0.05 M NaCl at different pH values (b).

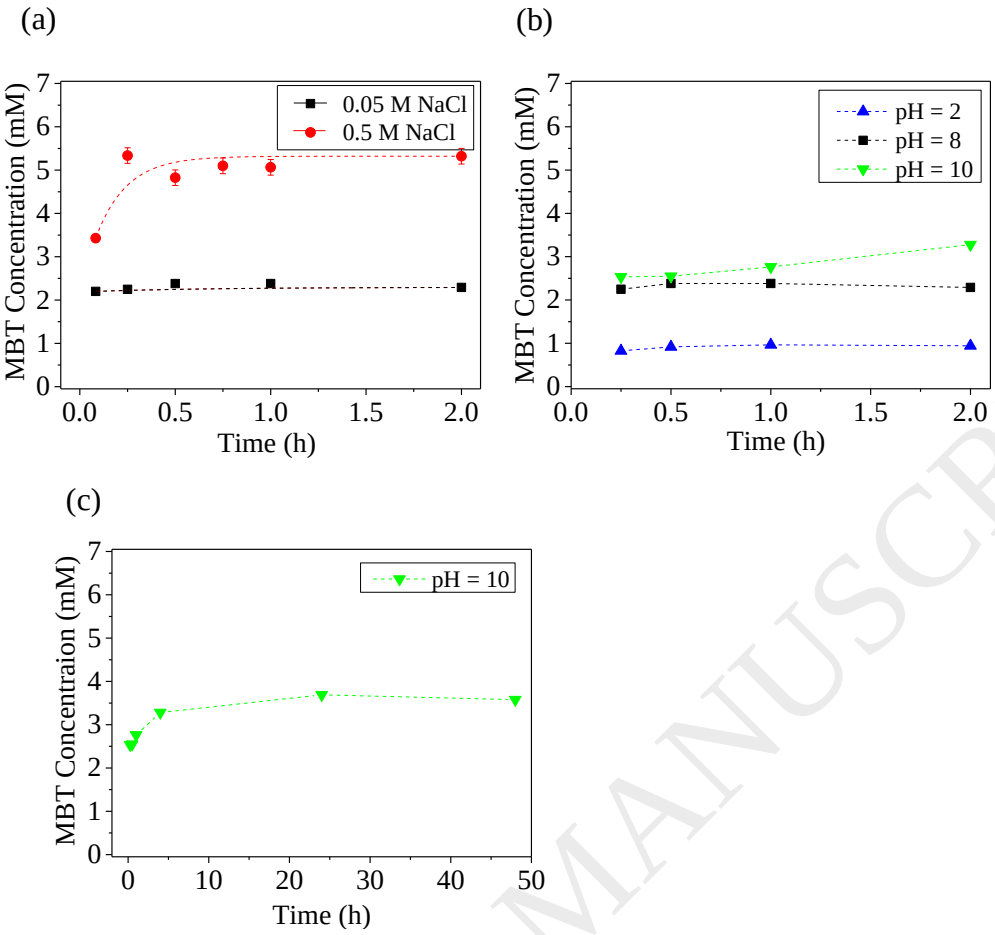

Figure 7. MBT release profiles at neutral pH in different NaCl concentrations (a) and in 0.05 M NaCl at different pH values (b).

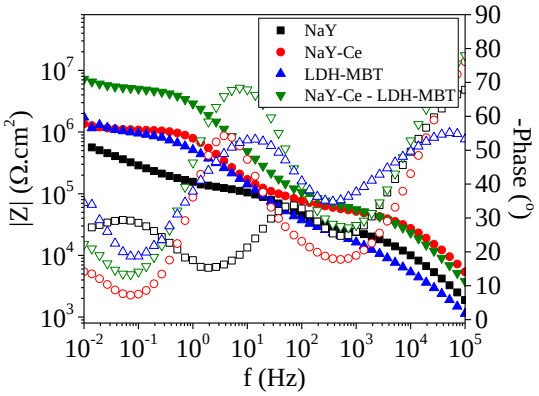

Figure 8. EIS spectra of waterborne epoxy coatings after 7 days exposure to 0.05 M NaCl.

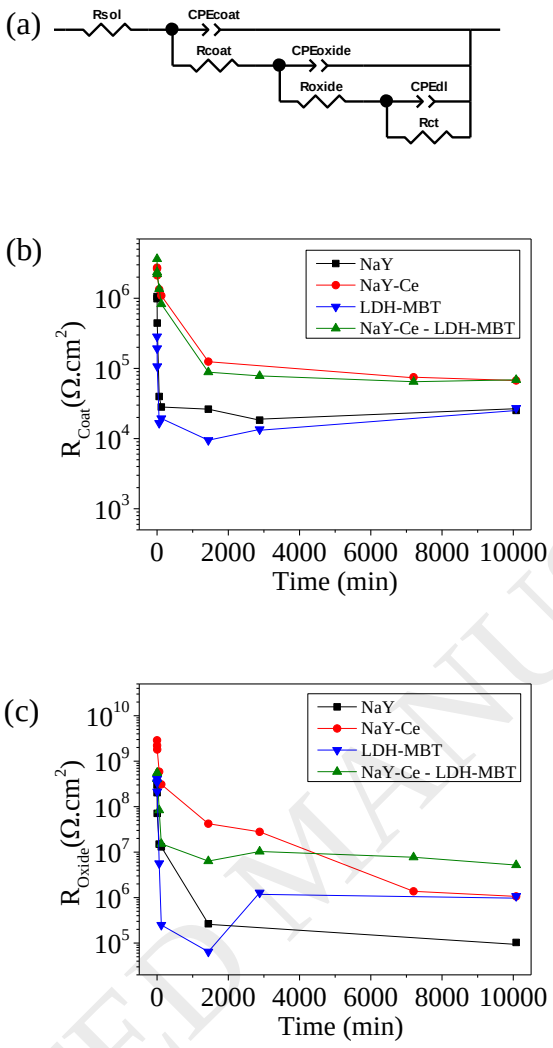

Figure 9. Equivalent circuit used to fit the experimental EIS data (a), and coating (R_{coat}) (b) and oxide (R_{oxide}) resistances (c) result of the fitting process of the waterborne coatings immersed for 7 days.

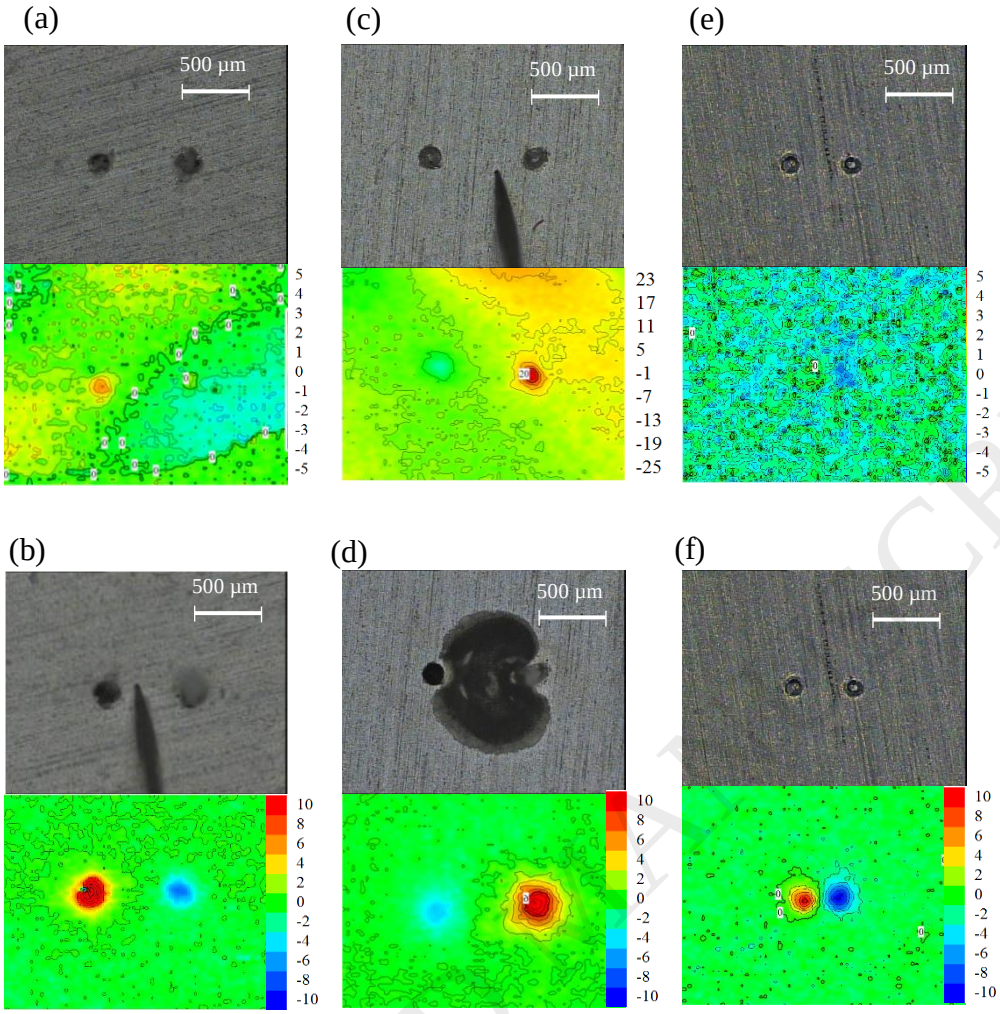

Figure 10. Optical micrographs and SVET maps of Ep-NaY-Ce (a) and (b), Ep-LDH-MBT (c) and (d) and Ep-NaY-Ce_LDH-MBT (e) and (f) after 1 and 7 days exposure to 0.05 M NaCl, respectively.

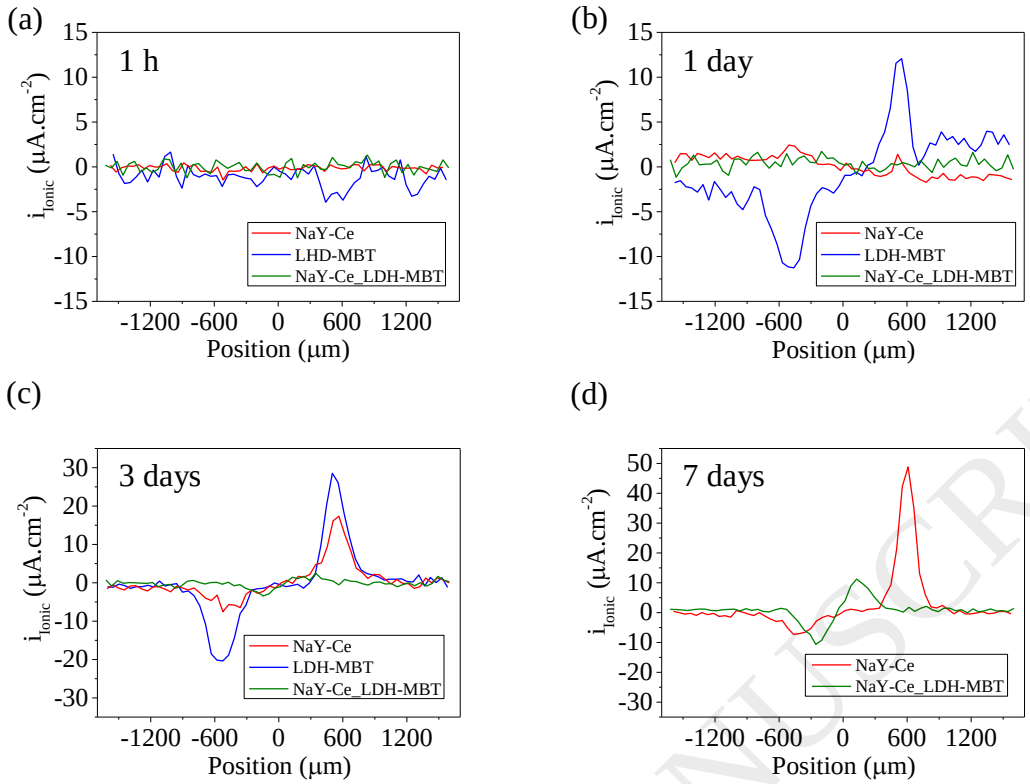

Figure 11. Ionic current density profiles of the extrinsic healing corrosion protective epoxy coatings after 1 h (a), 1 day (b), 3 days (c) and 7 days (d) exposure to 0.05 M NaCl, respectively.

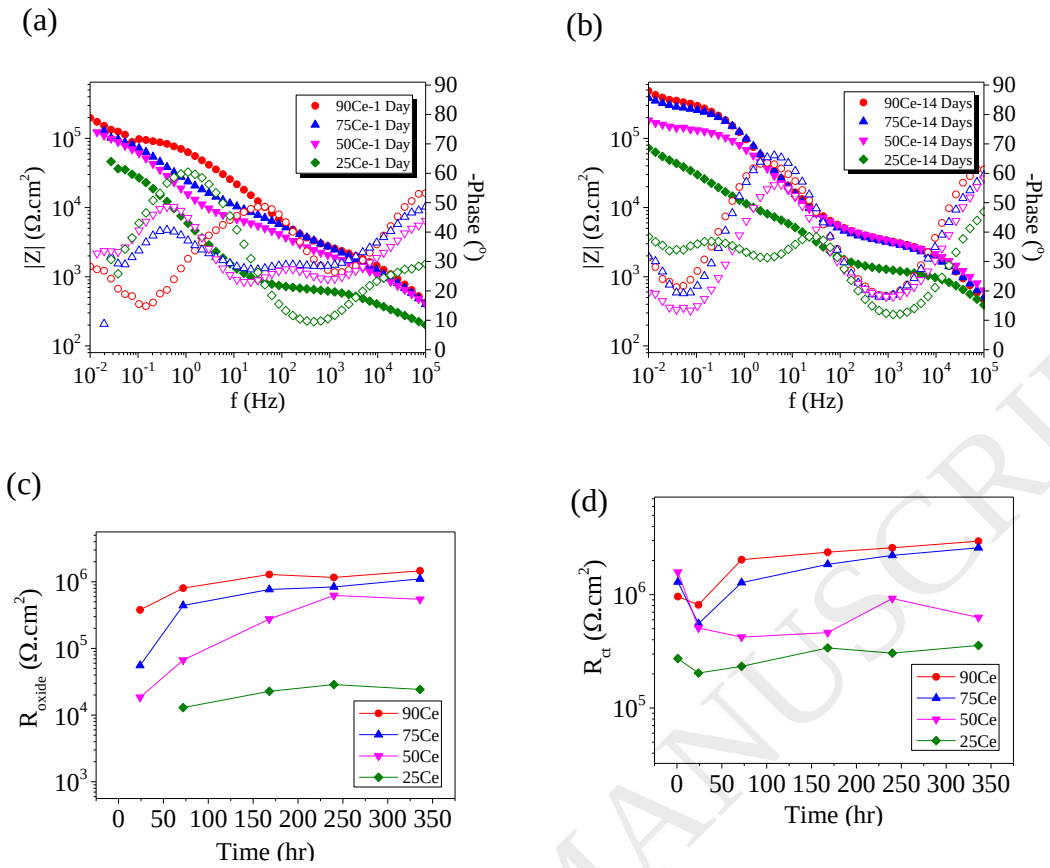

Figure 12. The EIS spectra of the epoxy coatings containing different ratios of NaY-Ce:LDH-MBT after 1 day (a) and 14 days (b) and the evolution of R_{oxide} (c) and $R_{ct.}$ (d) of the coating systems in 0.05 M NaCl. (90Ce, 75Ce, 50Ce and 25Ce represent NaY-Ce:LDH-MBT ratios of 90:10, 75:25, 50:50 and 25:75, respectively).

Table 1. Composition of the prepared extrinsic healing coatings.

Sample code	**Matrix**	**Micro-/Nano-container**	**inhibitor**
Ep-NaY	Waterborne epoxy resin	NaY	-
Ep-NaY-Ce		NaY	Ce^{3+}
Ep-LDH-MBT		LDH	MBT
Ep-NaY-Ce_LDH-MBT		NaY + LDH	Ce + MBT

Table 2. Charge transfer resistance (R_{ct}), fitting goodness (χ^2), inhibition efficiency (IE) and synergy parameter (S) for hybrid sol-gel and waterborne epoxy coatings after 1 and 7 days exposure to the electrolyte.

Table 2. Charge transfer resistance (R_{ct}), fitting goodness (χ^2), inhibition efficiency (η) and synergy parameter (S) for hybrid sol-gel and waterborne epoxy coatings after 1 and 7 days exposure to the electrolyte.

Time	Coating	χ^2	R_{ct} ($k\Omega.cm^2$)	η (-)	S (-)
1 Day	Ep-NaY	2.32×10^{-4}	3516	-	0.13
	Ep-NaY-Ce	1.04×10^{-3}	64410	0.95	
	Ep-LDH-MBT	4.19×10^{-4}	6870	0.49	
	Ep-NaY-Ce_LDH-MBT	6.83×10^{-4}	16560	0.79	
7 Days	Ep-NaY	2.32×10^{-4}	1067	-	2.14
	Ep-NaY-Ce	1.04×10^{-3}	1150	0.07	
	Ep-LDH-MBT	5.17×10^{-4}	2413	0.56	
	Ep-NaY-Ce_LDH-MBT	6.83×10^{-4}	5553	0.81	